Editors' Suggestion

3Q magnetic order with spatially alternating spin scalar chirality in overdoped $Co_{0.336}TaS_2$

Woonghee Cho,[1,2,*] Pyeongjae Park,[1,2,3,*] Chaebin Kim,[1,2] Yeochan An,[1,2] Kazuki Iida,[4] Ryoichi Kajimoto,[5] Sakib Matin,[6,7] Romain Sibille,[8] Scott A. Crooker,[9] and Je-Geun Park[1,2,10,†]

[1]*Center for Quantum Materials, Seoul National University, Seoul 08826, Republic of Korea*
[2]*Department of Physics and Astronomy, Seoul National University, Seoul 08826, Republic of Korea*
[3]*Materials Science & Technology Division, Oak Ridge National Laboratory, Oak Ridge, Tennessee 37831, USA*
[4]*Neutron Science and Technology Center, Comprehensive Research Organization for Science and Society (CROSS), Tokai, Ibaraki 319–1106, Japan*
[5]*Materials and Life Science Division, J-PARC Center, Japan Atomic Energy Agency, Tokai, Ibaraki 319–1195, Japan*
[6]*Center for Nonlinear Studies, Los Alamos National Laboratory, Los Alamos, New Mexico 87545, USA*
[7]*Theoretical Division, Los Alamos National Laboratory, Los Alamos, New Mexico 87545, USA*
[8]*PSI Center for Neutron and Muon Sciences, Paul Scherrer Institute, 5232 Villigen PSI, Switzerland*
[9]*National High Magnetic Field Laboratory, Los Alamos National Lab, Los Alamos, New Mexico 87545, USA*
[10]*Institute of Applied Physics, Seoul National University, Seoul 08826, Republic of Korea*

(Received 4 December 2025; revised 20 February 2026; accepted 31 March 2026; published 14 May 2026)

Co_xTaS_2 ($x \approx 1/3$) exhibits a spontaneous Hall effect from spin texture in antiferromagnets, with a tetrahedral triple-**Q** (3**Q**) order and uniform spin scalar chirality. Upon Co overdoping ($x > 1/3$), it undergoes a shift in magnetic ordering vectors from $\mathbf{Q}_m$ =(1/2, 0, 0) to (1/3, 0, 0). Interestingly, the spontaneous Hall effect disappeared in the overdoped regime, which was originally attributed to the loss of 3**Q** order. However, a question remains whether a new type of 3**Q** order can exist with alternating chirality in the overdoped regime. To address this, we investigated $Co_{0.336}TaS_2$ using inelastic neutron scattering (INS), neutron diffraction, and optical dichroism, and found that INS data and spin-wave simulations support a 3**Q** order with alternating chirality. Moreover, neutron diffraction data show field-independent Bragg peaks, while linear dichroism detects no in-plane anisotropy, consistent with threefold rotation symmetry. Our data support the scenario of an alternating-chirality 3**Q** order in $Co_{0.336}TaS_2$, canceling the spontaneous Hall effect. This study highlights a combined neutron-optical approach to identify complex spin textures.

DOI: 10.1103/d2yy-ntns

I. INTRODUCTION

One of the central questions in modern condensed matter physics is how topological properties emerge and manifest in magnetic systems with or without spin-orbit coupling. Among the most compelling examples are topological spin textures arising from multi-**Q** spin structures, where multiple magnetic ordering vectors coexist within a single magnetic configuration [1]. These structures give rise to exotic emergent properties that strongly influence the electronic responses of materials and have, consequently, become an active area of magnetism research [2–4]. A representative example is the topological Hall effect, which originates from the fictitious magnetic field induced by a noncoplanar spin configuration with net spin scalar chirality [2,5]. This emergent field is quantified by the so-called spin scalar chirality, defined as $\chi_{ijk} = \mathbf{S}_i \cdot (\mathbf{S}_j \times \mathbf{S}_k)$, where i, j, and k denote the sites of localized spins forming a three-site closed loop, and $\mathbf{S}_i$, $\mathbf{S}_j$, and $\mathbf{S}_k$ represent the corresponding localized spin moments at each site [1]. A well-known example of such a topological spin texture is the Skyrmion lattice (Sk-L) observed in two-dimensional (2D) hexagonal or tetragonal lattices, which typically arises from triple-**Q** or double-**Q** spin spirals or spin density waves [2,6–8].

Early discoveries of Sk-Ls were made in chiral magnets such as MnSi and Cu_2OSeO_3 [9–11], where the Sk-Ls exhibit long-wavelength periodicities typically in the range 10–100 nm. In contrast, many recent studies have identified Sk-Ls with much shorter atomic-scale periods—on the order of a few nm—in systems such as the Gd-based triangular lattice system Gd_2PdSi_3 [2]. While the stabilization of mesoscopic Sk-Ls in chiral crystals is generally attributed to the Dzyaloshinskii-Moriya (DM) interaction, invariably in conjunction with external magnetic fields and thermal fluctuations [9], this mechanism does not apply to systems with much shorter Sk-Ls—often observed even in centrosymmetric systems—and a different mechanism is required [2–4,6,12]. One promising theoretical framework invokes bilinear and four-spin exchange interactions, which can naturally arise from the Kondo lattice model in systems with itinerant electrons [13,14]. Notably, many of the characteristic features observed in these materials [2,3,7,8] are well captured by an effective spin Hamiltonian incorporating such higher-order interactions [3], underscoring the utility and validity of this approach in describing the atomic-scale Skyrmion lattice.

Recently, slightly off-stoichiometric $Co_{1/3-\delta}TaS_2$ ($\delta > 0$) has emerged as a representative experimental realization of

*These authors contributed equally to this work.
†Contact author: jgpark10@snu.ac.kr

the atomic-scale Sk-L, exhibiting a spontaneous Hall effect in the absence of net magnetization [5,7,8]. This Sk-L is characterized by a magnetic ordering vector located at the M points of the Brillouin zone, $\mathbf{Q}_m = (1/2, 0, 0)$ or its symmetry-equivalent vectors, which represents the short-wavelength limit of a Sk-L on a triangular lattice [7,15]. Remarkably, this magnetic structure exhibits sharp tunability with slight variations in the concentration of intercalated Co ions near $x = 1/3$ [16]. Detailed neutron diffraction studies on Co_xTaS_2 have revealed a composition-dependent evolution of the modulation vector: The slightly underdoped regime is associated with $\mathbf{Q}_m = (1/2, 0, 0)$, while the slightly overdoped regime corresponds to $\mathbf{Q}_m = (1/3, 0, 0)$ [16]. Importantly, the composition-sensitive changes in magnetic structure and transport properties observed in Co_xTaS_2 are an intrinsic feature of its underlying crystal structure, as similar behavior is also found in other intercalated transition metal dichalcogenides (TMDs). For example, Fe_xNbS_2 shows a composition-driven transition in the spin modulation vector from the stripe to zigzag order near $x = 1/3$ [17,18], and Co_xNbS_2 exhibits composition-dependent spontaneous Hall effect in the same doping vicinity [19,20]. Given that the properties of these systems can be easily tuned by intercalant concentration, structural disorder, such as vacancies or interstitial sites, is inevitable [21]. However, the narrow range of compositions investigated in those studies, including this work, makes it reasonable to attribute the origins of these transitions to intrinsic aspects, such as carrier doping and associated shifts in the Fermi surface, rather than disorder-driven effects.

The magnetic structure with $\mathbf{Q}_m = (1/3, 0, 0)$ in overdoped $Co_{1/3}TaS_2$ was initially interpreted as a 1**Q** spiral order, largely owing to the absence of a spontaneous Hall effect at the time [16]. Given the strong connection between tetrahedral 3**Q** magnetic order and the emergence of a spontaneous Hall effect in slightly underdoped $Co_{1/3}TaS_2$, the lack of such a spontaneous Hall effect in slightly overdoped $Co_{1/3}TaS_2$ has been taken as an indication of a topologically trivial 1**Q** spiral state. Here, in this paper, we argue that there is an alternative scenario in which the 3**Q** nature remains intact in the overdoped regime with $\mathbf{Q}_m = (1/3, 0, 0)$. The spin scalar chirality may adopt a spatially alternating configuration. In this case, although local spin scalar chiralities are nonzero, their spatial alternation leads to the cancellation of the net spin scalar chirality, which, although rarely observed, is compatible with the absence of a topological Hall effect. This possibility suggests that the overdoped phase of Co_xTaS_2, while lacking a macroscopic topological Hall effect, may still harbor a 3**Q** order with rich microscopic topology. Notably, similar scenarios involving chirality cancellation have been proposed in earlier studies on materials of a similar type [3,4,12,22,23]. To the best of our knowledge, however, no detailed investigation has been conducted to directly test the emergence of this hypothetical 3**Q** order with alternating chirality—an issue we aim to address in this work.

The unambiguous identification of multi-**Q** spin orders remains a significant experimental challenge, especially in the absence of clear macroscopic signatures such as the topological Hall effect. In such cases, conventional diffraction techniques are not often convincing, as their spatially averaged signals cannot distinguish between a multi-**Q** configuration and its multi-domain 1**Q** counterpart. To address this ambiguity, real-space imaging techniques, including Lorentz transmission electron microscopy (L-TEM) [11] and spin-polarized scanning tunneling microscopy (SP-STM) [12], have been used to visualize spin textures directly. However, these imaging methods face fundamental resolution limits as the spin modulation period approaches the atomic scale. In such regimes, complementary approaches become essential to ensure an error-free judgment on the conclusion. These include the analysis of momentum-resolved spectroscopic profiles or the use of probes sensitive to certain magnetic symmetries, such as optical linear dichroism [24]. Together, these methods can provide critical information about underlying spin textures, particularly in systems where real-space imaging and conventional diffraction are insufficient to resolve multi-**Q** order.

In this work, we propose and demonstrate an alternative approach based on inelastic neutron scattering [25–28], leveraging recent theoretical advances that enable the distinction between multidomain single-**Q** and single-domain multi-**Q** orders through their characteristic spin excitation spectra. This technique offers a momentum-resolved and complementary probe of complex magnetic textures, even in the absence of topological transport signatures. In addition to a spin-wave analysis, we conducted single-crystal neutron diffraction under an in-plane magnetic field that breaks the hexagonal symmetry and performed dichroism measurements—both linear and circular—to further corroborate the nature of the magnetic order. Taken together, these experimental results suggest that the spin configuration in overdoped $Co_{1/3}TaS_2$ is more consistent with a 3**Q** structure than a 1**Q** order. Our comprehensive approach thus establishes the presence of multi-**Q** spin ordering in this system and illustrates a powerful strategy for characterizing nontrivial magnetic states beyond conventional techniques.

II. METHODS

A. Single-crystal growth and bulk characterization

High-quality $Co_{1/3+\delta}TaS_2$ single crystals were synthesized using methods described in previous studies [16]. To produce the overdoped composition $Co_{0.336}TaS_2$, a solid-state reaction was performed using a cobalt: tantalum: sulfur molar ratio of 1.05–1.07:3:6, with a total batch mass of 5 g. A slight excess of cobalt (5–7%) was added to compensate for potential cobalt loss during synthesis. Given the extreme sensitivity of the magnetic properties to cobalt concentration, particular care was taken to characterize and select samples with high compositional precision.

Each crystal was examined using magnetometry (MPMS-XL5, Quantum Design, USA) and a scanning electron microscope (COXEM-EM30, COXEM, Korea) equipped with energy-dispersive x-ray spectroscopy (QUANTAX, Bruker, USA). Further screening for compositional homogeneity was conducted using magnetization and Raman spectroscopy. Notably, the distinct magnetization curves characteristic of the underdoped and overdoped regimes of $Co_{1/3\pm\delta}TaS_2$ allowed us to estimate the Co composition with greater accuracy

[16]. Only crystals exhibiting a sharp magnetic anomaly in the temperature range 35–41 K, indicative of the overdoped phase, were selected for the inelastic neutron scattering experiments. This selection criterion is further supported by earlier reports of a corresponding double anomaly in specific heat measurements at similar temperatures. Based on this protocol, we estimate the final composition variations of Co_xTaS_2 to range from $x = 0.333$ to $x = 0.338$. The fact that the temperature-dependent magnetic susceptibility of $x = 0.330$ and $x = 0.340$ is distinctly different from that of $x = 0.336$ (our target composition) renders the credibility to our estimate of the range [16].

B. Inelastic neutron scattering and spin-wave calculation

Crystals from the same synthesis batch displayed nearly identical magnetic behavior, indicating a high degree of compositional uniformity. Guided by previous reports on cobalt stoichiometry and bulk properties [16], we find our samples closest to $x = 0.336$ and therefore adopt "$Co_{0.336}TaS_2$" as the representative composition. For the inelastic neutron scattering experiments, the selected crystals (total mass of 4.2 g) were aligned on an aluminium plate using CYTOP adhesive (CTL-809M, Asahi Glass, Japan). The coaligned crystals were oriented in the (H H L)-horizontal geometry. The experiments were performed at the 4SEASONS time-of-flight spectrometer at J-PARC (Japan) [29], employing the repetition rate multiplication (RRM) technique [30]. Five incident neutron energies (35, 15, 8.3, 5.2, and 3.6 meV) were used with a chopper frequency of 150 Hz for $T = 7$ and 45 K. Experimental design and data reduction were carried out using the UTSUSEMI and HORACE software packages [31,32].

Finite-temperature Landau-Lifshitz-Gilbert (LLG) dynamics and linear spin wave theory (LSWT) calculations were performed using SU(N)NY simulation package [33] implemented in the Julia programming language [34]. For the calculation of $S_\perp(\boldsymbol{q}, E)$ at 45 K ($T > T_N$), simulations were carried on a $24 \times 24 \times 16$ supercell of the $Co_{1/3}TaS_2$ unit-cell (18 432 Co sites) with Langevin time step (dt) 0.02 me V^{-1} and a damping constant (λ) of 0.1. To ensure the thermally equilibrated starting configuration of paramagnetic phase, we first evolved the system for 10 000 Langevin steps and then computed $S_\perp(\boldsymbol{q}, E)$. The resulting spectra in the paramagnetic phases are averaged over five replicas. At 7 K below T_N, simulation used a $30 \times 30 \times 20$ supercell (36 000 Co sites) with the same Langevin time step and damping constant. In this case, $S_\perp(\boldsymbol{q}, E)$ was averaged over twenty replicas, and the LSWT calculation is computed from the 0 K structure. All $S_\perp(\boldsymbol{q}, E)$ datasets are multiplied by the Co^{2+} magnetic form factor and the neutron polarization factor to enable direct comparison with experimentally obtained data. Finally, instrumental resolution of energy and momentum transfer was incorporated with Gaussian broadening derived from the geometry of 4SEASONS spectrometer and full width at half maximum (FWHM) of observed nuclear Bragg peaks.

C. Single-crystal neutron diffraction under in-plane magnetic field

Single-crystal neutron diffraction under a magnetic field was performed using the ZEBRA thermal neutron diffractometer at the Swiss spallation neutron source SINQ. The sample was aligned in a 10 T vertical magnet (Oxford Instruments) with (HHL)-horizontal geometry. The beam of thermal neutrons was monochromatic using the (002) reflection of pyrolytic graphite.

D. Linear and circular dichroism measurement

For the optical studies of magnetic circular dichroism (MCD) and magnetic linear dichroism (MLD) experiments, which were recently shown to be sensitive to chiral and nematic antiferromagnetic phases in underdoped $Co_{1/3}TaS_2$ [35], single-crystal samples were mounted in a helium vapor, strain-free environment on a variable-temperature insert (2–300 K) within a 7 T magneto-optical cryostat (Oxford Spectromag) equipped with direct optical access. Wavelength-tunable probe light was generated from a xenon lamp and spectrally filtered through a 300-mm spectrometer. The probe beam was mechanically chopped at a low frequency of 137 Hz, linearly polarized, and then polarization-modulated using a photoelastic modulator (PEM).

To measure MCD, the polarization was modulated between right- and left-circular states (quarter-wave modulation) at a frequency of 50 kHz. For MLD, the polarization was modulated between orthogonal linear states (half-wave modulation) at a frequency of 100 kHz. The probe beam was weakly focused onto the sample surface with a spot size of ~1 mm under near-normal incidence. The reflected light intensity was detected by an avalanche photodiode, amplified, and demodulated using dual lock-in amplifiers. MCD was measured as the normalized difference in reflectance between right- and left-circularly polarized light, defined as $(I_R - I_L)/(I_R + I_L)$. Similarly, MLD was quantified as $(I_\phi - I_{\phi+90^\circ})/(I_\phi + I_{\phi+90^\circ})$, where ϕ is the angle of the linear polarization of the probe beam. MCD is closely related to the magneto-optical Kerr effect (MOKE) and is sensitive to magnetic orders that induce a nonzero off-diagonal conductivity $\sigma_{xy}(\omega)$, such as ferromagnetism or specific antiferromagnetic phases [36–38]. In contrast, MLD is sensitive to anisotropy in the in-plane optical conductivity, e.g., $\sigma_{xx}(\omega)$–$\sigma_{yy}(\omega)$, which may arise from single-**Q** (stripe-like) AFM order [35,39].

III. RESULTS AND DISCUSSION

A. Parameterization and underlying Hamiltonian of 3Q order for Q = (1/3, 0, 0)

Figure 1(a) shows the crystal structure of ideal $Co_{1/3}TaS_2$, and Fig. 1(b) shows the magnetic susceptibility of the $x = 0.336$ sample ($T_N = 35$ K). Figure 1(c) presents the momentum-resolved elastic neutron scattering profile at 7 K (4SEASONS), with magnetic Bragg peaks at $\mathbf{Q}_m = (1/3, 0, 0)$ and symmetry-equivalent positions [$\mathbf{Q}_m = (0, 1/3, 0)$, $(1/3, -1/3, 0)$]. Such a pattern can, in principle, arise from either (i) three domains of a single-**Q** (1**Q**) order or (ii) a noncoplanar triple-**Q** (3**Q**) order [see Fig. 1(d)]. In the 1**Q** scenario, the magnetic order with $\mathbf{Q}_m = (1/3, 0, 0)$ can be described as a three-sublattice spin spiral propagating along the a* direction. This configuration features a coplanar spin texture and has twofold rotational symmetry (C_{2z}) about the crystallographic c axis. In contrast, the 3**Q** structure arises from the

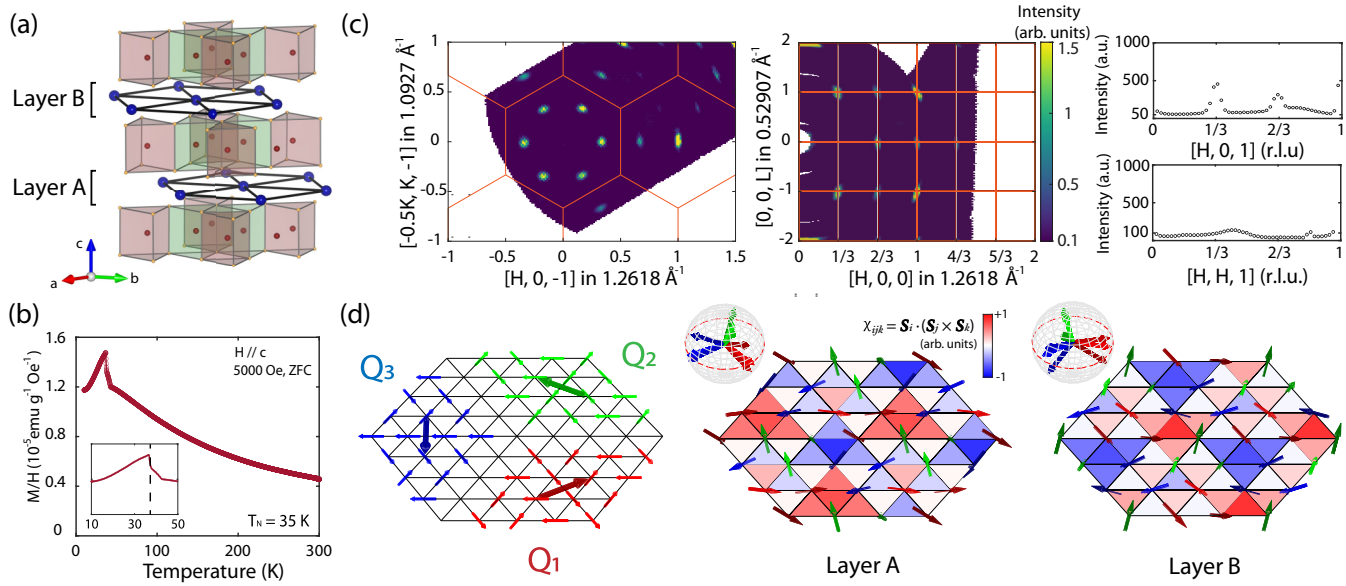

FIG. 1. Proposed spin order for $Co_{0.336}TaS_2$, constrained by crystal structure and highly commensurate magnetic Bragg peaks and corresponding phase transition observed via bulk susceptibility measurement. (a) A crystallographic unit cell of $Co_{1/3}TaS_2$. The light green Ta-S prism color denotes structural chirality induced by the insertion of a 3d transition metal. (b) Temperature-dependent magnetization of single-crystal $Co_{0.336}TaS_2$ with H $\parallel$ c. (c) Experimentally measured magnetic Bragg peaks (7 K) observed at BL01 4SEASONS, J-PARC MLF. (d) Schematics of candidate spin order for $Co_{0.336}TaS_2$. The overall spin orientation is rotated for better visualization, such that the main spin components lie within the *ab* plane. (Left) 1**Q** spiral order with three domains, where thick arrows represent the direction of modulation vector $\mathbf{Q}_i$ ($i = 1,2,3$) in real space, and (center and right) noncoplanar 3**Q** order with spin texture in A and B sublattices, with overall spin direction illustrated in the corresponding unit sphere above.

superposition of three spin modulations described by $\mathbf{Q}_m = (1/3, 0, 0)$ and the two other symmetry-equivalent wave vectors. The resulting spin texture is noncoplanar and preserves threefold rotational symmetry (C_{3z}) about the c axis. These symmetry distinctions are central to differentiating between the two candidate states and motivate the subsequent experimental analysis.

To gain insight into the stabilization mechanism of the 3**Q** magnetic structure arising from $\mathbf{Q}_m = (1/3, 0, 0)$, we introduce the phenomenological spin Hamiltonian under consideration [28],

$$H = \sum_n \sum_\delta J_\delta \boldsymbol{S}_n \cdot \boldsymbol{S}_{n+\delta} + \sum_n \sum_\delta K_\delta (\boldsymbol{S}_n \cdot \boldsymbol{S}_{n+\delta})^2, \qquad (1)$$

where n represents site position, $\boldsymbol{S}_n$ denotes spin for each site n, and J_δ and K_δ are exchange and biquadratic interactions for given displacement δ. Within the framework of bilinear Heisenberg interactions, magnetic ordering with $\mathbf{Q}_m = (1/3, 0, 0)$ can be stabilized by appropriately tuning the relative magnitudes of beyond nearest-neighbor interactions. This framework yields two energetically degenerate states: (i) a triple-domain 1**Q** structure and (ii) a coplanar 3**Q** structure. However, we emphasize a crucial constraint that must be satisfied in real space: the uniformity of spin length across all lattice sites, i.e., $|\boldsymbol{S}_j| = S$ across all j. In a general 3**Q** superposition, arbitrary choices of spin components for each modulation vector typically violate this condition. To satisfy the spin-length constraints, one must select specific spin components for each **Q**-vector in the 3**Q** state. When this condition is met, both the triple-domain 1**Q** and the coplanar 3**Q** structure remain exactly degenerate, satisfying the local spin length conservation within the bilinear Heisenberg model. The spin configuration that satisfies this condition was first obtained from numerical energy minimization of the bilinear Heisenberg Hamiltonian and then parameterized in reciprocal space to express its analytic form. An explicit expression for the coplanar 3**Q** structure is thus given in the following form:

$$\begin{aligned}
\boldsymbol{S}_j &= \boldsymbol{S}_{\mathbf{Q}_1} e^{i\mathbf{Q}_3 \cdot \boldsymbol{x}_j} + \boldsymbol{S}_{\mathbf{Q}_2} e^{i\mathbf{Q}_3 \cdot \boldsymbol{x}_j} + \boldsymbol{S}_{\mathbf{Q}_3} e^{i\mathbf{Q}_3 \cdot \boldsymbol{x}_j} + (\text{c.c}), \\
\boldsymbol{S}_{\mathbf{Q}_1} &= S(1 \quad -i \quad 0)^T, \quad \mathbf{Q}_1 = \left(\frac{1}{3}, 0, 0\right), \\
\boldsymbol{S}_{\mathbf{Q}_2} &= S\left(-\cos\left(\frac{\pi}{3}\right) - i\sin\left(\frac{\pi}{3}\right)\cos\left(\frac{\pi}{6}\right) - i\sin\left(\frac{\pi}{6}\right) 0\right)^T, \\
\mathbf{Q}_2 &= \left(0, \frac{1}{3}, 0\right), \\
\boldsymbol{S}_{\mathbf{Q}_3} &= S\left(-\cos\left(\frac{\pi}{3}\right) - i\sin\left(\frac{\pi}{3}\right)\cos\left(\frac{\pi}{6}\right) - i\sin\left(\frac{\pi}{6}\right) 0\right)^T, \\
\mathbf{Q}_3 &= \left(\frac{1}{3}, -\frac{1}{3}, 0\right). \qquad (2)
\end{aligned}$$

At the level of the bilinear Heisenberg Hamiltonian, the 1**Q** and coplanar 3**Q** structures are perfectly degenerate in energy. Although general proof for the uniqueness of this 3**Q** structure is beyond the present scope, our energy-minimization results consistently converge to either 1**Q** or the 3**Q** structure presented above. The solution above exhibits equal intensity among the three ordering vectors $\mathbf{Q}_i$ ($i = 1, 2, 3$) along with maintaining the local spin-length conservation confirms that it represents a valid realization of the 3**Q** structure. Furthermore, the energy degeneracy implies that a transition between the

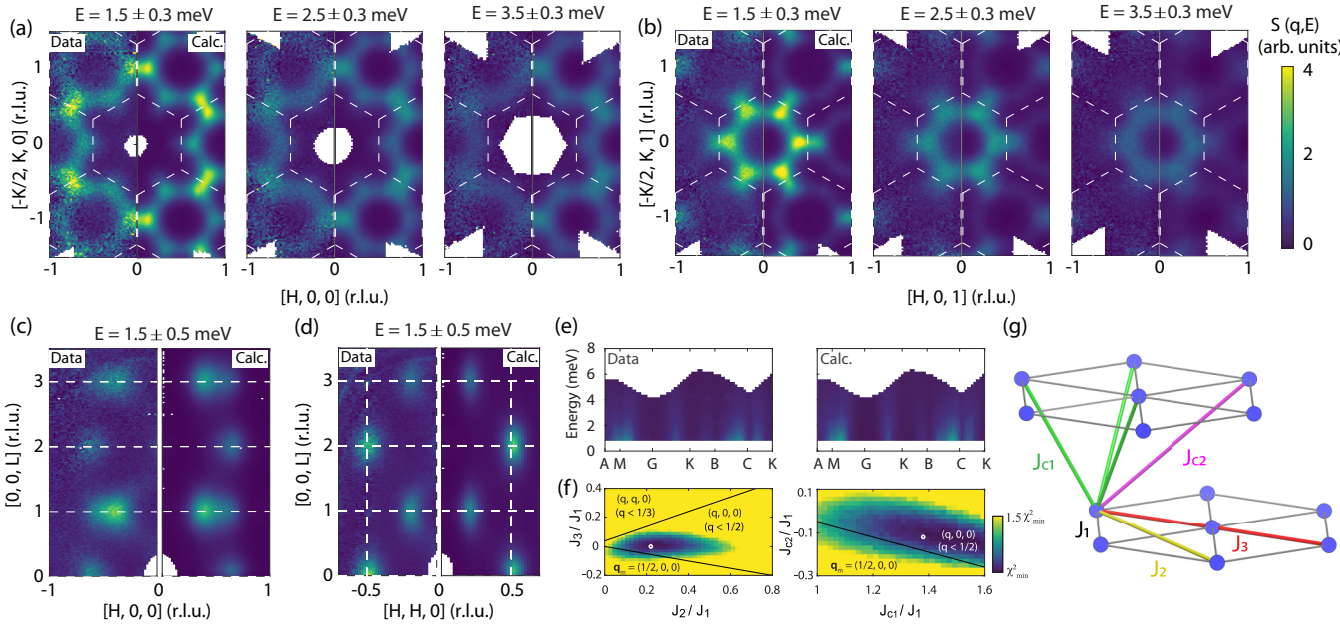

FIG. 2. Comparison of the paramagnetic excitation spectra measured at $T = 45$ K with theoretical calculations from a best-fit spin Hamiltonian. (a)–(e) Paramagnetic scattering spectra for various momentum and energy slices, measured at 45 K (slightly above $T_N = 35$ K), where a finite temperature LLG simulation is also performed with $T = 45$ K. The simulation effectively captures energy-momentum transfer at the paramagnetic region for the wide Brillouin zone, indicating that the system in the paramagnetic phase can be well described by a classical LLG simulation with isotropic Heisenberg interactions. (f) Parameter dependence of the fitting error for the paramagnetic scattering data. The presence of a well-defined global minimum across a wide parameter range demonstrates the robustness and reliability of the extracted exchange interaction parameters. Notably, the same energy-momentum transfer data for $Co_{0.325}TaS_2$ show that the stable modulation vector is $\mathbf{Q}_m = (1/2, 0, 0)$ [28]. (g) Exchange interaction paths are considered in the calculation for intralayer exchange interaction J_n and interlayer exchange interaction J_{cn}.

two structures requires overcoming a finite energy barrier, confirming the structural stability of the 3**Q** structure.

However, this degeneracy is lifted by the inclusion of a positive biquadratic interaction between nearest-neighbor spins, which further stabilizes another noncoplanar 3**Q** ground state relative to the coplanar 3**Q** ground state. This term naturally arises from higher-order interactions in the Kondo lattice model and serves as the microscopic origin for the stabilization of the noncoplanar 3**Q** ground state [13]. In this noncoplanar configuration, a small but finite Fourier component is present at $\mathbf{Q} = (1/3, 1/3, 0)$, in a zero-temperature calculation. It arises from higher-order harmonics of the three fundamental wave vectors ($\mathbf{Q}_1$, $\mathbf{Q}_2$, and $\mathbf{Q}_3$), which give rise to the noncoplanarity in the spin texture. Yet, within the relevant regime of biquadratic interaction strength considered in this work (see Fig. 3), its magnitude is less than 1% of the nominal magnitude of the primary reflections described by $\mathbf{Q}_m = (1/3, 0, 0)$. The estimated neutron diffraction intensity of these higher harmonic signals from the model calculation is far below the background intensity [see Fig. 1(c)]. Based on the background-subtracted data relative to the paramagnetic phase (45 K) and taking the 2σ statistical fluctuation of the background as a criterion, the accessible upper limit for the magnetic reflection intensity at $\mathbf{Q} = (1/3, 1/3, 1)$ was estimated to be 4% relative to the primary $\mathbf{Q} = (1/3, 0, 1)$ peak intensity.

Nevertheless, we found that the long-wavelength behavior of the spin-wave calculation clearly captures the difference as discussed below. A similar role of higher harmonics in stabilizing Skyrmion lattices has been discussed in theoretical studies based on bilinear-biquadratic spin Hamiltonians [40]. In this case, the addition of a positive biquadratic term favors the noncoplanar 3**Q** structure with alternating spin chirality as the magnetic ground state without modifying the bilinear Heisenberg interaction. Notably, recent experimental studies have also underscored the role of higher-order spin interactions in stabilizing atomic-scale multi-**Q** phases [3,4].

For $Co_{1/3}TaS_2$, such higher-order terms are naturally justified within the Kondo lattice model, where conduction electrons mediate magnetic exchange between localized spins [14]. It is further supported by the crystal structure: CoS_6 octahedrons are fully isolated, with a nearest-neighbor Co-Co distance of 5.74 Å, well beyond Hill's limit [41], confirming the absence of direct Co-Co wavefunction overlap. Consequently, the magnetic interactions in this system are predominantly mediated by itinerant electrons in the TaS_2 layers, an essential feature of the Kondo lattice model. Previous experimental work on underdoped $Co_{1/3}TaS_2$ estimated the biquadratic interaction to be approximately 6% of J_1 (where J_1 represents the nearest-neighbor bilinear exchange interaction) [28]. Based on this result, we conservatively adopt an upper bound of 6% for the biquadratic interaction in the overdoped system and perform our theoretical analysis accordingly.

For completeness, we note that applying the bilinear-biquadratic Hamiltonian for $Co_{1/3}TaS_2$ leads to two distinct spin configurations for the A and B sublattices. It originates from the space group of ideal $Co_{1/3}TaS_2$, $P6_322$ (no. 182), where the Cobalt ion occupies the $2c$ Wyckoff positions

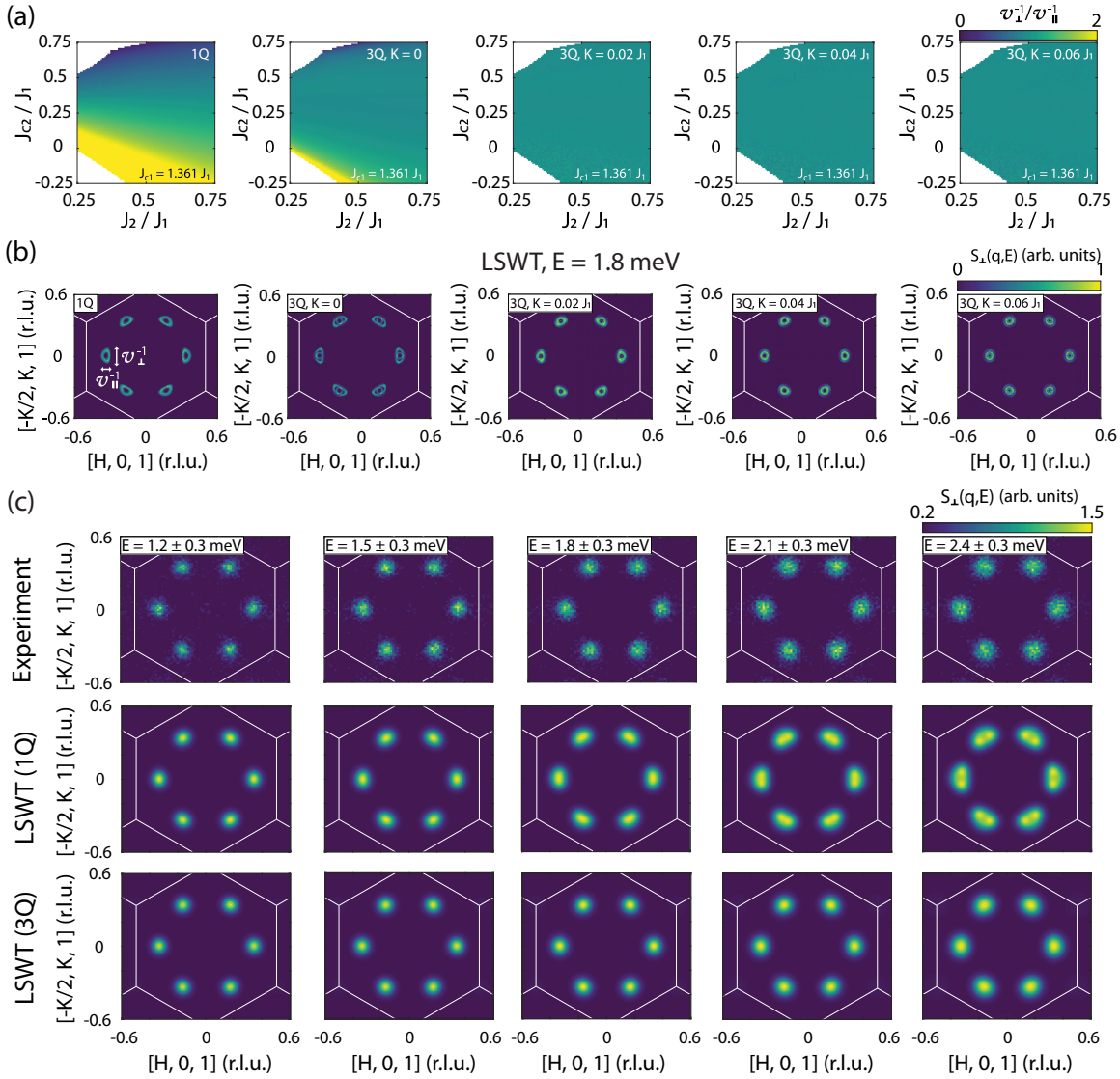

FIG. 3. Distinguishing single-**Q** and triple-**Q** magnetic ground states by comparing theoretical spin-wave spectra with experimental data. (a) Long-wavelength spin-wave velocity anisotropy $v_{\perp}^{-1}/v_{||}^{-1}$ calculated from LSWT for given structure (1**Q** and 3**Q**) and intensity of biquadratic interaction K for 1NN interaction for given J_2 and J_{c2}. To stabilize the $\mathbf{Q} = (1/3,0,0)$ as a stable modulation vector, J_3 is calculated from Eq. (4). (b) Constant energy slices of energy transfer E = 1.8 meV for [HKL] = [001] region calculated from LSWT using a parameter set given in Table II. For a clear demonstration of the effect of biquadratic interaction in 3**Q** order, the experimental broadening effect is not considered. (c) Long-wavelength limit spin-wave for (first row) experimental result (second row) equally populating 1**Q** helical order domain summation and (third row) 3**Q** order with the spin texture of [HKL] = [001] plane. Experimental results are collected at $T = 7$ K and simulation results are obtained using LLG dynamics at $T = 7$ K. Experimental broadening is applied with an FWHM obtained from the magnetic Bragg peak. The used parameter set is given in Table II. $K = 0.06J_1$ is additionally considered for the 3**Q** order.

forming two sublattices (A and B) of the triangular lattice. These sublattices are connected by a 6_3-screw operation and form two distinct magnetic ion sites within the unit cell. This enables the distinct spin configuration for the A and B sublattices even though the ordering vector $\mathbf{Q} = (1/3, 0, 0)$ implies no modulation along the c axis. Figure 1(a) illustrates the obtained 3**Q** spin structures for the A and B sublattices of the triangular lattice with spin directions mapped onto the unit sphere. Whereas the 1**Q** spiral structure involves only a phase difference within each sublattice, the 3**Q** structure exhibits an alternating pattern between the A and B sublattices owing to antiferromagnetic coupling between the A and B sublattices. This alteration, in addition to the alteration of the scalar spin chirality within a single layer, leads again to a vanishing total spin scalar chirality and net magnetization.

B. Inelastic neutron scattering and long wavelength spinwave anisotropy

To experimentally determine the ground state of overdoped $Co_{1/3}TaS_2$, we compared inelastic neutron scattering spectra with theoretical predictions obtained using LSWT and LLG dynamics simulations for various candidate spin configurations. To gain insights into the underlying exchange

interaction in overdoped $Co_{1/3}TaS_2$, we first analyzed the excitation spectra in the paramagnetic phase, commonly known as paramagnetic diffuse scattering. This approach offers two key advantages. First, it enables the estimation of the bilinear interaction profile without bias toward a specific modulation vector or an assumed 1**Q** or 3**Q** nature of the ordered phase. Second, as demonstrated in previous studies [42,43], the paramagnetic regime minimizes the limitations of semiclassical spin dynamics theory, such as spin-wave renormalization effects that may become significant in quantum spin systems or in cases of complex noncollinear magnetic order. Therefore, the analysis of the spin dynamics in the paramagnetic state provides a robust foundation for constructing an effective magnetic model that can be consistently applied to calculate the spin-wave spectra of multiple candidate ground states. This methodology has been successfully applied in recent studies across a range of systems [28,42–46], demonstrating its reliability in capturing the interaction parameters of the magnetic Hamiltonian. In our case, we adopted an isotropic Heisenberg model with five distinct exchange parameters (J_1, J_2, J_3, J_{c1}, J_{c2}) corresponding to interactions among five different types of Co–Co ion pairs [see Fig. 2(g)]. The Hamiltonian is expressed as

$$\begin{aligned} H &= H_{\text{intra}} + H_{\text{inter}}, \\ H_{\text{intra}} &= \frac{1}{2}\sum_i \sum_n^{\text{intra}} J_n\left[\left(\boldsymbol{S}_i^A \cdot \boldsymbol{S}_{i+n}^A\right) + \left(\boldsymbol{S}_i^B \cdot \boldsymbol{S}_{i+n}^B\right)\right], \\ H_{\text{inter}} &= \frac{1}{2}\sum_i \sum_n^{\text{inter}} J_{cn}\left(\boldsymbol{S}_i^A \cdot \boldsymbol{S}_{i+n}^B\right), \end{aligned} \tag{3}$$

where J_n denotes the nth neighbor intralayer exchange interaction within the same sublattice (A or B), and J_{cn} denotes the nth neighbor interlayer exchange interaction between different sublattices (A–B). The summation $\sum_n^{\text{intra}}$ and $\sum_n^{\text{intra}}$ run over the corresponding neighbor shell n; the factor $\frac{1}{2}$ is considered to avoid double counting [see Fig. 2(g) for the mapping J_1, J_2, J_3 and J_{c1}, J_{c2}]. By convention, we use $J > 0$ for antiferromagnetic interaction and $J < 0$ for ferromagnetic interaction.

Paramagnetic scattering data were collected using an incident energy $E_i = 8.3$ meV. The measurements were performed at $T = 45$ K, and corresponding simulations were carried out using finite-temperature LLG dynamics at the same temperature to ensure consistency. To efficiently optimize the parameters of the five-dimensional Heisenberg Hamiltonian, we first employed the Bayesian optimization algorithm implemented in Python [47], using a Gaussian process as the surrogate model [48]. This probabilistic framework enables efficient exploration of the parameter space while minimizing the number of costly simulation evaluations. Following this initial optimization, we manually refined and validated the results by comparing them against neighboring regions in parameter space to confirm that the global minimum was reliably identified.

Figures 2(a)–2(e) show the calculated paramagnetic scattering intensity maps based on the optimized model Hamiltonian (see Table I). At the same time, Fig. 2(f) presents the corresponding goodness-of-fit landscape across two-dimensional slices of the five-dimensional parameter space.

TABLE I. Optimal parameter set for the five exchange interactions (J) derived from the paramagnetic phase. $S = 3/2$ is assumed for the spin length. The uncertainty of the parameter (σ_J) is determined based on 10% increase from χ^2_{min} by varying each parameter independently while keeping others fixed. The reported values represent the larger value between the positive and negative deviations. The relative magnitudes of J_1 are also listed for easier comparison with theoretical magnetic phase diagrams in Fig. 2(f). The obtained χ^2 value for the paramagnetic phase refinement (Fig. 2) is approximately 2221, representing the minimized residual between the experimental data (Fig. 2) and the theoretical model.

	J_1	J_2	J_3	J_{c1}	J_{c2}
J (meV)	1.311	0.303	0.004	1.784	–0.134
σ_J (meV)	±0.093	±0.079	±0.052	±0.157	±0.052
J/J_1	1	0.2312	0.0031	1.3611	−0.1024

These maps confirm the presence of a well-defined global minimum in the chi-square map, supporting the robustness of the extracted parameter set. Notably, the optimized model predicts a magnetic modulation vector $\mathbf{Q}_m = (q, 0, 0)$, with $q < 1/2$. This is in contrast to the previous result on underdoped $Co_{1/3}TaS_2$, where the exchange parameters determined using the same methodology yielded $\mathbf{Q}_m = (1/2, 0, 0)$ [28]. Notably, the same constant-energy and energy-momentum slices of the paramagnetic excitation spectrum were used in the analysis of overdoped $Co_{1/3}TaS_2$ here, as in the previous study of underdoped $Co_{1/3}TaS_2$ [28]. Remarkably, this difference in the predicted modulation vectors suggests that the paramagnetic diffuse scattering signal successfully captures, to some extent, the composition-dependent evolution of magnetic interactions and the resulting magnetic orders with distinct magnetic modulation vectors.

The successful reproduction of the paramagnetic scattering spectra using our optimized Hamiltonian confirms that this approach provides a reasonable estimate of magnetic interactions. However, a limitation arises too: The fitted parameter from the paramagnetic scattering does not directly reproduce the modulation vector $\mathbf{Q}_m = (1/3, 0, 0)$ observed experimentally in the ordered phase. Instead, the model predicts $\mathbf{Q}_m \approx (0.4, 0, 0)$. Such discrepancies between Hamiltonians derived from paramagnetic scattering and those governing the ordered phase have also been reported in a few systems, including systems with nearly or weakly incommensurate modulation vectors [44,46]. In our case, prior reports indicate that the transition from $\mathbf{Q}_m = (1/2, 0, 0)$ to $\mathbf{Q}_m = (1/3, 0, 0)$ occurs sharply with only a small change in Co composition, suggesting that commensurability may arise from a lock-in mechanism. Here, we note that the experimentally observed $\mathbf{Q}_m$ coincides with $(1/3, 0, 0)$ within the momentum resolution of the spectrometer [see Fig. 1(c)]. While a full understanding of this mechanism lies beyond the scope of the present study, it implies that the commensurate $\mathbf{Q}_m = (1/3, 0, 0)$ may be stabilized by effects beyond the classical Heisenberg model.

To phenomenologically model the ordered phase with $\mathbf{Q}_m = (1/3, 0, 0)$, we slightly adjust the exchange parameters from those estimated at $T > T_N$ (see Table II). Although the high-temperature fit does not yield a quantitatively accurate magnetic ground state, it still provides a reliable range for

TABLE II. Hamiltonian parameter used to reproduce the spin wave spectra in the ordered phase. The uncertainty of the parameter (σ_J) is estimated based on the qualitative agreement between the simulated and experimental data. J_3 is automatically adjusted from given J_{c1} and J_{c2} to stabilize the modulation vector $\mathbf{Q}_m = (1/3, 0, 0)$. The obtained χ^2 value for the ordered phase is approximately 467, derived from a comparison between the experimental inelastic neutron scattering spectra at 7 K and spin dynamics simulations over a consistent momentum-energy transfer range given in Fig. 2.

	J_1	J_2	J_3	J_{c1}	J_{c2}
J (meV)	1.451	0.611	0.0143	1.975	0.207
σ_J (meV)	±0.15	±0.073	N/A	±0.145	±0.116
J/J_1	1	0.4212	0.0099	1.3611	0.1424

the five relevant interaction parameters. Enforcing $\mathbf{Q}_m = (1/3, 0, 0)$ within our Heisenberg model requires imposing a new constraint that relates J_3 to the interplanar interactions J_{c1} and J_{c2} (see Appendix A for the details),

$$J_3 = \frac{1}{2}\left[1 - \frac{FG - \frac{FJ_{c2}}{2} + 2GJ_{c2}}{\sqrt{F^2 - 2FG + 4G^2}}\right],$$
$$F = (J_{c1} + J_{c2}),$$
$$G = \left(J_{c1} - \frac{J_{c2}}{2}\right). \tag{4}$$

This condition can be derived using the Luttinger-Tisza method [49] and was validated through simulated annealing and spin-wave calculations. For the current scope of isotropic Heisenberg interactions described by five-parameters (J_1, J_2, J_3, J_{c1}, J_{c2}) with antiferromagnetic J_1 and J_{c1}, the stable ordering vector appears along the ΓM line, [$\mathbf{Q}$ = (q, 0, 0) with $0 \leqslant q \leqslant 1/2$], or the ΓK line [$\mathbf{Q}$ = (q, q, 0) with $0 \leqslant q \leqslant 1/3$], in reciprocal space. Specifically, for $\mathbf{Q} = (1/3, 0, 0)$, we found that, within the physically reasonable regime ($|J_2| < |J_1|$), the stable ordering vector remains unchanged under variations in J_2, provided that $\mathbf{Q} = (1/3, 0, 0)$ continues to be the global energy minimum over competing states such as $\mathbf{Q}$ = (q, q, 0) or $\mathbf{Q} = (0, 0, 0)$. In other words, starting from the region of parameter space where $\mathbf{Q} = (1/3, 0, 0)$ is the global energy minimum, variation in J_2 alone does not affect the location of the stable ordering vector, unless the energy minimum shifts discretely to other competing ordering vectors such as $\mathbf{Q}$ = (q, q, 0) or $\mathbf{Q} = (0, 0, 0)$. In our approach, we adopt a scheme in which J_2, J_{c1}, and J_{c2} are systematically tuned, and J_3 is consequently determined by the constraint.

Under this condition, the Heisenberg Hamiltonian yields a perfect energy degeneracy between the triple-domain 1**Q** and coplanar 3**Q** structures for $\mathbf{Q}_m = (1/3, 0, 0)$. It allows both configurations to emerge as ground states under the same exchange parameters in theoretical calculations. To lift this degeneracy and stabilize a noncoplanar ground state, we introduced an additional positive biquadratic interaction K between first nearest-neighbor (1NN) spin pairs,

$$H_K = K \sum_i \sum_n^{\text{intra}-1NN} (\boldsymbol{S}_i \cdot \boldsymbol{S}_{i+n})^2. \tag{5}$$

We then investigated how variations in K affect the spin-wave spectra, particularly for the noncoplanar 3**Q** configuration. With increasing K, the spin structure becomes increasingly noncoplanar, leading to a nonzero local spin scalar chirality χ_{ijk}, which is spatially modulated in an alternating pattern, as previously discussed [see Fig. 1(d), where $K = 0.06\, J_1$ is used].

To differentiate among the candidate magnetic ground states based on their spin dynamics, we analyzed the anisotropy of spin-wave velocities in the long-wavelength limit. A previous study [28] demonstrated the effectiveness of this approach in distinguishing between a triple-domain 1**Q** state and a single-domain 3**Q** configuration, as these two scenarios exhibit qualitatively distinct spin-wave dispersions near the magnetic ordering vector. Specifically, in the long-wavelength regime, the acoustic spin-wave branches in a 1**Q** structure are expected to display pronounced directional anisotropy in velocity, reflecting the uniaxial nature of the modulation. In contrast, a 3**Q** state, formed by a superposition of symmetry-equivalent wave vectors, should give rise to a nearly isotropic spin-wave velocity profile in momentum space.

In this context, spin-wave velocity anisotropy can be quantified by comparing the long-wavelength spin-wave velocities along two orthogonal directions: (1, 0, 0) (in reciprocal lattice units), which is parallel to the magnetic ordering vector $\mathbf{Q}_m$ and (–1, 2, 0), which is perpendicular to it. The spin-wave velocities, denoted as $v_\parallel$ and $v_\perp$, are defined as following form, evaluated at $\mathbf{Q}_m = (1/3, 0, 0)$. Here, $\omega(\mathbf{q})$ is the spin-wave energy obtained from linear spin-wave theory (LSWT). We evaluate $v_\parallel$ and $v_\perp$ for the Goldstone mode by finite-difference method for $\omega(\mathbf{q})$ with sufficiently small spacing [$q_{\parallel(\perp)} = 0.025\, \boldsymbol{a}^*$] from $\mathbf{Q}_m = (1/3, 0, 0)$,

$$v_{\parallel(\perp)} = \lim_{|\boldsymbol{q}_{\parallel(\perp)}| \to 0} \frac{\omega(\mathbf{Q}_m + \boldsymbol{q}_{\parallel(\perp)}) - \omega(\mathbf{Q}_m)}{|\boldsymbol{q}_{\parallel(\perp)}|}. \tag{6}$$

Figure 3(a) presents the calculated velocity anisotropy across a $J_2/J_1 - J_{c2}/J_1$ parameter space, whereas J_3 and J_{c1} were chosen based on the values extracted from our paramagnetic diffuse scattering analysis and the constraint imposed by Eq. (4). The 1**Q** structure can exhibit a wide range of velocity anisotropies, depending on the specific values of the exchange parameters. The isotropic velocity profile ($v_\parallel/v_\perp \sim 1$) is only realized within a specific choice of parameters within the space, suggesting that a strong directional dependence of spin-wave dispersion is generically expected in a 1**Q** state.

By systematically increasing the strength of K from 0 to $0.06J_1$, we examined how the long-wavelength velocity profile—calculated using LSWT—changes, through the low-energy constant energy slice of the spin-wave spectra [Figs. 3(a) and 3(b)]. Introducing finite K to the Hamiltonian, which stabilizes the non-coplanar 3**Q** ground state over the 1**Q** or coplanar 3**Q** states, gradually drives the spectrum toward an isotropic velocity profile. Understanding the effect of K requires recognizing how it alters the local spin texture. Despite the 3**Q** character, the coplanar 3**Q** structure stabilized at $K = 0$ does not provide the same relative spin alignments between six nearest-neighbor bonds—a key requirement for achieving the isotropic velocity profile as proposed in the previous study

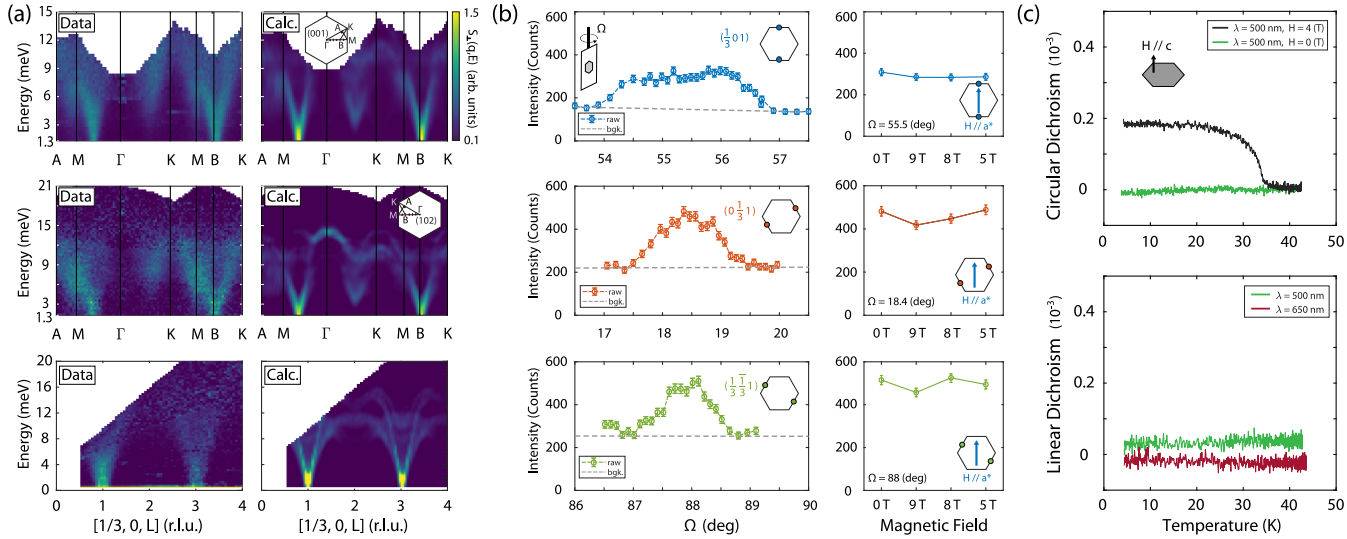

FIG. 4. Probing the triple-**Q** (3**Q**) magnetic state of $Co_{0.336}TaS_2$ from spin dynamics, magnetic-field response, and symmetry of the magnetic structure. (a) Fitted spin-wave spectra (7 K) for the full Brillouin zone. $K = 0.06J_1$ is applied for the calculation. Experimental broadening is explicitly accounted for through the full width at half maximum (FWHM) of the magnetic Bragg peak, and the energy resolution is estimated from the information provided by the beamline tools. (b) A rocking scan from single-crystal neutron diffraction and peak intensity tracing for a finite in-plane field along the [100] direction, with the collimator removed, is used to estimate the absolute intensity of each peak. (c) (Top) Linear dichroism measurement for $\lambda = 500$ nm (green) and $\lambda = 650$ nm (red) at $H_{ext} = 0$ T and (bottom) circular dichroism measurement at $\lambda = 500$ nm and $H_{ext} = 4$ T (light green) and $H_{ext} = 0$ T (green), field along c axis.

[28]. As a result, the coplanar 3**Q** phase can exhibit sizable velocity anisotropy. On the other hand, increasing K gradually induces noncoplanarity in the ground state, driving it toward a configuration with more uniform relative spin alignments among the six NN pairs. Indeed, this trend is clearly shown in Fig. 3(a), where the velocity anisotropy becomes significantly suppressed once K becomes nonzero, in agreement with the scenario proposed in Ref. [28]. Thus, the degree of velocity isotropy directly reflects the noncoplanar 3**Q** nature of the ground state among feasible candidate states in our model. Notably, our inelastic neutron scattering (INS) data exhibit a nearly isotropic profile that closely matches the LSWT prediction for finite K [$K = 0.06\ J_1$ for Fig. 3(c)] [Figs. 3(a)–3(c)].

After establishing the trend in long-wavelength spinwave anisotropy for each candidate spin structure within the parameter region estimated from the paramagnetic diffuse scattering, we next focus on the full spin-wave spectra across the Brillouin zone. By applying modest adjustments to the model Hamiltonian, guided by the experimentally determined modulation vector $\mathbf{Q}_m$ and slightly rescaling the overall energy scale, we could reproduce the observed spin-wave features. While paramagnetic diffuse scattering provided a robust baseline, a direct application of the refined parameter to the ordered state proved insufficient, as it failed to predict the modulation vector $\mathbf{Q} = (1/3, 0, 0)$. This prompted us to adjust the exchange parameters for the ordered phase, including an overall energy scale increase of approximately 11% and refined tuning of each exchange parameter. In particular, the value of J_3 was adjusted under constraints imposed by the fixed $\mathbf{Q}_m = (1/3, 0, 0)$, as discussed earlier. From LSWT's perspective, these adjustments (such as the sign reversal of J_{c2}) were required to reproduce the experimentally observed spinwave spectra. For instance, this requires the hardening of spinwave energy at M-point [$\mathbf{Q} = (1/2, 0, 0)$] and energy minima along Γ-K [$\mathbf{Q} = (q, q, 0)$ ($q < 1/3$)]. The precise lock-in of $\mathbf{Q}_m$ to commensurate (1/3, 0, 0) and the necessity of distinct parameter sets for the ordered and paramagnetic phases may suggest a reorganization of exchange interactions upon entering the ordered phase, which cannot be fully captured in our temperature-independent spin Hamiltonian.

The fitted spin-wave spectra are shown in Figs. 3(c) and 4(a). Interestingly, compared to high-energy spinwave excitation modes, which are far from magnetic Bragg peaks and appear relatively insensitive to whether the underlying spin configuration is 1**Q** or 3**Q**, we find that constant-energy slices at low energies exhibit pronounced differences between the two structures. This highlights that, although both configurations yield similar global spectra when fitted with a common set of exchange parameters, the long-wavelength spinwave anisotropy patterns revealed in constant-energy maps are highly sensitive to whether the spin order is 1**Q** or 3**Q**. As illustrated in Fig. 3(c), this distinction is especially visible for the [HKL] = [HK1]. Notably, the only difference between the two calculations lies in the inclusion of a positive biquadratic interaction $K = 0.06\ J_1$ in the 3**Q** case.

C. Single-crystal neutron diffraction and linear (circular) dichroism

To further support the presence of a 3**Q** magnetic order, we performed single-crystal neutron diffraction measurements under an applied in-plane magnetic field—an approach often employed to distinguish genuine multi-**Q** states from multidomain single-**Q** scenarios. The experiments were conducted at the ZEBRA instrument, PSI-SINQ, with rocking scans carried out for $\mathbf{Q}_{m1} = (1/3, 0, 1)$ and its symmetry-equivalent

positions: zero field (H = 0) and finite field (H = 9, 8, 5 T), applied along the reciprocal lattice vector **a***. These results are summarized in Fig. 4(b). In the case of a triple-domain 1**Q** structure, an applied magnetic field is expected to induce domain repopulation owing to the field-induced energy difference between the three domains. The measured diffraction intensities, obtained by integrating the peak area and applying the Lorentz factor correction, showed negligible change between zero and finite fields. This field independence suggests the absence of domain repopulation within the range of applied fields and is more consistent with a single-domain 3**Q** structure that preserves threefold rotational symmetry.

We also performed complementary optical linear and circular dichroism (LD/CD) measurements under a magnetic field to provide additional insights into the symmetry and chiral properties of the magnetic ground state in overdoped $Co_{1/3}TaS_2$. Figure 4(c) presents the temperature dependence of the LD and CD signals. Recent work has demonstrated that linear dichroism is a highly sensitive probe for detecting symmetry breaking associated with stripe-like (1**Q**) magnetic ordering [24,35,39,50]. In particular, spatially resolved LD measurements have shown the appearance of three distinct nematic domains with reduced C_{2z} symmetry, with optical responses rotated by 120° on triangular or hexagonal lattices, which can be understood as magnetic domains of 1**Q** orders that break threefold rotational symmetry [35,39,50–54].

In contrast to previous studies, our measurement of overdoped $Co_{1/3}TaS_2$ shows no discernible LD signal appearing across the magnetic transition. This absence of LD strongly suggests that the magnetic structure retains its threefold rotational symmetry in the ordered state [50,51]. To interpret this result more rigorously, we relate the LD responses to the dielectric tensor, focusing on the rotational symmetry properties of the candidate magnetic configurations. The two spin structures under consideration—the 1**Q** spiral order and the 3**Q** noncoplanar order—can be distinguished by their symmetry with respect to the crystallographic *c* axis. Based on point group symmetry analysis and assuming effective time-reversal symmetry (motivated by the absence of a spontaneous Hall effect), the dielectric tensor in the two-dimensional *ab* plane for each magnetic configuration can be expressed as follows (see Appendix B for a detailed symmetry analysis):

$$\epsilon = \begin{cases} \begin{pmatrix} \epsilon_{xx} & 0 \\ 0 & \epsilon_{yy} \end{pmatrix} & \text{for } 1Q \text{ order} \\ \begin{pmatrix} \epsilon_{xx} & 0 \\ 0 & \epsilon_{xx} \end{pmatrix} & \text{for } 3Q \text{ order} \end{cases}. \tag{7}$$

This anisotropic dielectric tensor is directly related to the anisotropy of in-plane optical conductivity, which underlies the LD signal. Consequently, the absence of a measurable LD signal below the magnetic ordering temperature is consistent with a 3**Q** order proposed for overdoped $Co_{1/3}TaS_2$. By contrast, three-state domains of the LD signal have been observed in other intercalated TMD, notably in Fe_xNbS_2, where distinct magnetic domain configurations break rotational symmetry and can be selectively repopulated under external perturbations, such as uniaxial strain or current pulses [50,55]. A very similar observation has been reported for underdoped $Co_{1/3}TaS_2$, where symmetry breaking induced by nematic domains was effectively captured in resistivity anisotropy [56] or more directly by the LD signal [35]. The absence of such behavior in overdoped $Co_{1/3}TaS_2$ further supports the scenario of a single-domain, symmetry-preserving 3**Q** ground state. Further investigations of this aspect, based on resistivity measurements under uniaxial strain, will validate the magnetic symmetry of the system.

In contrast to the absence of noticeable change in the LD signal, magnetic circular dichroism (CD) measurements clearly detect the magnetic transition, only under an external out-of-plane magnetic field (H_{ext} = 4 T) [Fig. 4(c)]. Consistent with the absence of a spontaneous Hall effect in overdoped $Co_{1/3}TaS_2$ [16], σ_{xy} (H = 0), we observe no measurable CD response in the zero-field environment. This situation is distinct from the underdoped $Co_{1/3}TaS_2$, where a spontaneous Hall effect provides a clear one-to-one correspondence between the CD signal and the topological Hall effect [35].

As demonstrated in Fig. 4(c), our finite-field CD measurement is clearly sensitive to the onset of long-range magnetic order in overdoped $Co_{1/3}TaS_2$. A complete understanding of the origin of the signal, whether from a field-induced canted moment or another origin, requires further investigation. However, a notable connection can be made to the transport properties of overdoped $Co_{1/3}TaS_2$. Prior study reported a distinct change in the Hall coefficient across the magnetic phase transition in overdoped $Co_{1/3}TaS_2$ [16]. The analogous trend observed in our finite-field CD measurement suggests a potential correspondence with the nontrivial behavior in the Hall coefficient.

Our findings, interpreted through the lens of a spin Hamiltonian, suggest that higher-order four-spin interactions persist in Co_xTaS_2 throughout its composition-dependent phase diagram, even across abrupt changes in the magnetic modulation vector induced by slight deviations from a stoichiometric limit. This robustness of the multi-**Q** structure could seemingly contrast with some previous reports, such as the case of iron-based superconductors, where such multi-**Q** structures are reported to be stabilized only within a narrow doping regime [57]. Yet, it should be noted that the covered composition range in this work—merely 1% or 2% of Co vacancy of excess Co—is also still narrow enough, and further under- or overdoping will likely modify or destabilize the multi-**Q** magnetic orders. Experimentally, multi-**Q** spin structures of this type are more commonly observed in systems with large spin magnitudes, such as Gd^{3+}- or Eu^{2+}-based compounds (S = 7/2, L = 0), where biquadratic terms arise naturally as perturbative corrections and scale as $O(S^4)$ [2–4,6]. This context raises a compelling question: How do significant higher-order interactions emerge in the magnetism from 3*d* transition metal systems, where spin sizes are relatively small? One possible explanation lies in the local structure and bonding environment of Co^{2+} ions in Co–S octahedra. The relatively localized nature of Co^{2+} 3*d* electrons, combined with large nearest-neighbor Co–Co distances exceeding 5 Å, may suppress conventional exchange mechanisms, such as superexchange interactions, and enhance the relative importance of higher-order interactions, including biquadratic interactions. Recent advances in *ab initio* calculations of biquadratic exchange [58] provide a promising

avenue for uncovering the microscopic origin of these interactions in cobalt-intercalated TMDs. A deeper theoretical understanding of this mechanism could significantly expand our knowledge of exotic spin textures in 3*d*-based systems. The observed significant composition-driven magnetic structure change in underdoped and overdoped $Co_{1/3}TaS_2$ exhibits striking parallels with the related compound $Co_{1/3}NbS_2$, which has also been reported to host a tetrahedral 3**Q** order [8] and to display sample-dependent spontaneous Hall effects [19,20]. These similarities suggest a potentially common underlying mechanism governing the composition and sample sensitivity across cobalt-intercalated TMDs. In this broader context, the spin Hamiltonian framework and inelastic neutron scattering methodology developed in the present study offer a powerful guideline for exploring $Co_{1/3}NbS_2$. Applying this methodology could reveal composition-induced shifts in the magnetic ordering vector, similar to those observed in Co_xTaS_2, and thereby deepen our understanding of the intricate interplay between electronic structure, spin texture, and topological transport responses in cobalt-intercalated TMDs.

Finally, regarding the microscopic origin of the sharp tunability of the magnetic modulation vector, we note a relevant precedent in $Fe_{1/3}NbS_2$, where a composition-induced shift in the spin ordering vector has been experimentally observed [17] and later attributed to the presence or absence of charge order [18]. This finding suggests that a similar charge-related mechanism may be at play in $Co_{1/3\pm\delta}TaS_2$, potentially contributing to the modulation of the vector shift and the emergence of distinct spin textures across doping levels. Investigating the coupling between charge and spin degrees of freedom, particularly the role of electronic instability or charge order, represents a promising avenue for future research. Such studies would further illuminate the rich interplay among lattice, charge, and spin in 3*d* transition metal-intercalated TMDs, thereby deepening our understanding of the mechanisms driving their complex magnetic and topological behaviors.

IV. CONCLUSIONS

In conclusion, we combined inelastic neutron scattering, single-crystal neutron diffraction, and linear and circular dichroism measurements to elucidate the spin structure of intercalated $Co_{0.336}TaS_2$. Our comprehensive analysis suggests that the magnetic ground state of the overdoped $Co_{1/3}TaS_2$ adopts a 3**Q** configuration with spatially alternating spin-scalar chirality χ_{ijk}. This finding provides insights into the complex spin textures and multi-**Q** magnetic states, particularly their connections to topologically nontrivial phenomena in condensed matter systems. Theoretically, such real-space modulations of spin-scalar chirality have long been predicted in various model Hamiltonians [59,60], and several materials have been proposed as potential hosts of these exotic spin states [3,12,22]. Our experimental results provide evidence for such a state in overdoped $Co_{0.336}TaS_2$ and underscore the effectiveness of combining neutron scattering with dichroism-sensitive optical probes to resolve magnetic structures accurately. This integrated approach provides a powerful framework for future studies of topological magnetism in intercalated transition metal dichalcogenides and other frustrated spin systems.

ACKNOWLEDGMENTS

We acknowledge Maxim Avdeev, Hanjin Noh, Myung Joon Han, Ki Honn Lee, Younjung Jo, Kee Hoon Kim, and Cristian Batista for their helpful discussions. The neutron-scattering experiment at the Japan Proton Accelerator Research Complex was performed under the user program (Proposal No. 2023A0036). P.P. acknowledges support by the U.S. Department of Energy, Office of Science, Basic Energy Sciences, Materials Science and Engineering Division. S.A.C. gratefully acknowledges support from the Los Alamos LDRD program. The National High Magnetic Field Laboratory is supported by National Science Foundation Grant No. DMR-2128556 and the State of Florida. This work was supported by the Samsung Science & Technology Foundation (Grant No. SSTF-BA2101-05). One of the authors (J.-G.P.) is partly funded by the Leading Researcher Program of the National Research Foundation of Korea (Grant No. RS-2020-NR049405). This work has been partially supported by U.S. DOE Grant No. DE-FG02-13ER41967. ORNL is managed by UT-Battelle, LLC, under Contract No. DE-AC05-00OR22725 for the U.S. Department of Energy.

This manuscript has been authored by UT-Battelle, LLC, under contract DE-AC05-00OR22725 with the US Department of Energy (DOE). The US government retains and the publisher, by accepting the article for publication, acknowledges that the US government retains a nonexclusive, paid-up, irrevocable, worldwide license to publish or reproduce the published form of this manuscript, or allow others to do so, for US government purposes. DOE will provide public access to these results of federally sponsored research in accordance with the DOE Public Access Plan [61].

DATA AVAILABILITY

The data that support the findings of this article are not publicly available. The data are available from the authors upon reasonable request.

APPENDIX A: LUTTINGER-TISZA ANALYSIS FOR DETERMINING THE MAGNETIC ORDERING VECTOR

The Luttinger-Tisza method provides a standard framework for determining the stable magnetic ordering vector by minimizing the Fourier-transformed exchange interaction $J(\boldsymbol{k})$ from real-space exchange interactions $J(\boldsymbol{r})$,

$$J(\boldsymbol{k}) = \sum_{\boldsymbol{r}} J(\boldsymbol{r}) e^{i\boldsymbol{k}\cdot\boldsymbol{r}}. \tag{A1}$$

For a single-sublattice system, $J(\boldsymbol{k})$ itself directly represents the magnetic energy to be minimized. For the systems with multiple magnetic sublattices, however, this term becomes a matrix form $J_{ab}(\boldsymbol{k})$, where each element corresponds to the coupling between spins on the ath and bth sublattices,

$$J_{ab}(\boldsymbol{k}) = \sum_{\boldsymbol{r}} J_{ab}(\boldsymbol{r}) e^{i\boldsymbol{k}\cdot\boldsymbol{r}}. \tag{A2}$$

In this case, $J_{ab}(\boldsymbol{k})$ becomes a Hermitian matrix, where the minimum eigenvalue $\lambda_{\min}(\boldsymbol{k})$ represents the relevant magnetic energy. In the case of an AB-stacked triangular lattice with five Heisenberg exchange parameters (J_1, J_2, J_3, J_{c1}, J_{c2}), the interaction matrix takes the form

$$J_{ab}(\boldsymbol{k}) = \begin{pmatrix} J_{\text{intra}}(\boldsymbol{k}) & J_{\text{inter}}(\boldsymbol{k}) \\ J_{\text{inter}}(\boldsymbol{k}) & J_{\text{intra}}(\boldsymbol{k}) \end{pmatrix}. \tag{A3}$$

The intra- and interlayer parts of the Fourier-transformed exchange interaction are expressed in the following forms:

$$\begin{aligned} J_{\text{intra}}(\boldsymbol{k}) &= \sum_{n}^{\text{intra}-1NN} J_1 e^{i\boldsymbol{k}\cdot\boldsymbol{r}_n} + \sum_{n}^{\text{intra}-2NN} J_2 e^{i\boldsymbol{k}\cdot\boldsymbol{r}_n} + \sum_{n}^{\text{intra}-3NN} J_3 e^{i\boldsymbol{k}\cdot\boldsymbol{r}_n}, \\ J_{\text{inter}}(\boldsymbol{k}) &= \sum_{n}^{\text{inter}-1NN} J_{c1} e^{i\boldsymbol{k}\cdot\boldsymbol{r}_n} + \sum_{n}^{\text{inter}-2NN} J_{c2} e^{i\boldsymbol{k}\cdot\boldsymbol{r}_n}. \end{aligned} \tag{A4}$$

For the high-symmetry direction, $\mathbf{k} = (q, 0, 0)$, the eigenvalues $\lambda_{\pm}(\boldsymbol{k})$ can be obtained analytically as

$$\begin{aligned} \lambda_{\pm}(q) = {} & 2J_1 \cos(q) + J_2[2\cos(q) + \cos(2q)] + 2J_3 \cos(2q) \\ & \pm \sqrt{(J_{c1}+J_{c2})^2 + 4(J_{c1}+J_{c2})\cos(q)(J_{c1}+J_{c2}\cos(q)) + 4(J_{c1}+J_{c2}\cos(q))^2}. \end{aligned} \tag{A5}$$

To test whether $\mathbf{Q} = 2\pi(1/3, 0, 0)$ can host an extremum, we first impose the stationarity condition, which is a necessary (but not sufficient) requirement,

$$\left.\frac{d\lambda_{\min}(q)}{dq}\right|_{q=\frac{2\pi}{3}} = 0. \tag{A6}$$

This leads to the following constraint among J_3, J_{c1}, and J_{c2}. We note that the apparent absence of J_2 in this relation originates from the insertion of $\mathbf{Q} = 2\pi(1/3, 0, 0)$, where the coefficient of J_2 to the stationary condition effectively cancels out. In the general case, however, the constraint takes the form of an interrelated equation involving J_2, J_3, J_{c1}, and J_{c2},

$$J_3 = \frac{1}{2}\left[J_1 - \frac{(J_{c1}+J_{c2})\left(J_{c1}-\frac{1}{2}J_{c2}\right) - \frac{J_{c2}}{2}(J_{c1}+J_{c2}) + 2J_{c2}\left(J_{c1}-\frac{J_{c2}}{2}\right)}{\sqrt{(J_{c1}+J_{c2})^2 - 2(J_{c1}+J_{c2})\left(J_{c1}-\frac{J_{c2}}{2}\right) + 4\left(J_{c1}-\frac{J_{c2}}{2}\right)^2}}\right]. \tag{A7}$$

The constraint derived above guarantees that $\mathbf{k} = 2\pi(1/3, 0, 0)$ satisfies the stationarity condition of $\lambda_{\min}(\boldsymbol{k})$. Provided that this stationary point is also the global minimum in reciprocal space, $\mathbf{k} = 2\pi(1/3, 0, 0)$ is realized as the stable magnetic ordering vector.

APPENDIX B: SYMMETRY CONSIDERATION IN THE LINEAR DICHROISM MEASUREMENT

The original crystal structure of $Co_{1/3}TaS_2$ has a space group $P6_322$ (No. 182). Let us consider the point group symmetry of the space group. There exists both twofold and threefold rotation symmetry for the c axis, as well as twofold rotation symmetry for the a and a^* axes, along with time-reversal symmetry. Considering a threefold rotation and time-reversal symmetry, the dielectric tensor takes the form of a diagonal matrix,

$$\epsilon = \begin{pmatrix} \epsilon_{xx} & 0 & 0 \\ 0 & \epsilon_{xx} & 0 \\ 0 & 0 & \epsilon_{zz} \end{pmatrix}. \tag{B1}$$

If we consider a spin order of $1\mathbf{Q}$ helical order of $\mathbf{Q}_m = (1/3, 0, 0)$, we lose a threefold rotation symmetry for the c axis. Considering the effective time-reversal symmetry of the system from the absence of spontaneous Hall effect, we could obtain the form of a dielectric tensor as follows:

$$\epsilon = \begin{pmatrix} \epsilon_{xx} & 0 & 0 \\ 0 & \epsilon_{yy} & 0 \\ 0 & 0 & \epsilon_{zz} \end{pmatrix}. \tag{B2}$$

In contrast to the $1\mathbf{Q}$ spiral order, the $3\mathbf{Q}$ order still preserves threefold rotation symmetry for the c axis. This yields a form of the dielectric tensor that is equivalent to Eq. (B1).

[1] N. Nagaosa and Y. Tokura, Topological properties and dynamics of magnetic skyrmions, Nat. Nanotechnol. **8**, 899 (2013).

[2] T. Kurumaji *et al.*, Skyrmion lattice with a giant topological Hall effect in a frustrated triangular-lattice magnet, Science **365**, 914 (2019).

[3] H. Yoshimochi *et al.*, Multistep topological transitions among meron and skyrmion crystals in a centrosymmetric magnet, Nat. Phys. **20**, 1001 (2024).

[4] N. D. Khanh *et al.*, Nanometric square skyrmion lattice in a centrosymmetric tetragonal magnet, Nat. Nanotechnol. **15**, 444 (2020).

[5] P. Park *et al.*, Field-tunable toroidal moment and anomalous Hall effect in noncollinear antiferromagnetic Weyl semimetal $Co_{1/3}TaS_2$, npj Quantum Mater. **7**, 42 (2022).

[6] R. Takagi *et al.*, Square and rhombic lattices of magnetic skyrmions in a centrosymmetric binary compound, Nat. Commun. **13**, 1472 (2022).

[7] P. Park *et al.*, Tetrahedral triple-Q magnetic ordering and large spontaneous Hall conductivity in the metallic triangular antiferromagnet $Co_{1/3}TaS_2$, Nat. Commun. **14**, 8346 (2023).

[8] H. Takagi *et al.*, Spontaneous topological Hall effect induced by non-coplanar antiferromagnetic order in intercalated van der Waals materials, Nat. Phys. **19**, 961 (2023).

[9] S. Mühlbauer *et al.*, Skyrmion lattice in a chiral magnet, Science **323**, 915 (2009).

[10] A. Neubauer *et al.*, Topological Hall effect in the *A* phase of MnSi, Phys. Rev. Lett. **102**, 186602 (2009).

[11] S. Seki, X. Z. Yu, S. Ishiwata, and Y. Tokura, Observation of skyrmions in a multiferroic material, Science **336**, 198 (2012).

[12] J. Spethmann *et al.*, SP-STM study of the multi-Q phases in $GdRu_2Si_2$, Phys. Rev. Mater. **8**, 064404 (2024).

[13] Y. Akagi, M. Udagawa, and Y. Motome, Hidden multiple-spin interactions as an origin of spin scalar chiral order in frustrated Kondo lattice models, Phys. Rev. Lett. **108**, 096401 (2012).

[14] S. Hayami, R. Ozawa, and Y. Motome, Effective bilinear-biquadratic model for noncoplanar ordering in itinerant magnets, Phys. Rev. B **95**, 224424 (2017).

[15] Z. Wang and C. D. Batista, Skyrmion crystals in the triangular Kondo lattice model, SciPost Phys. **15**, 161 (2023).

[16] P. Park *et al.*, Composition dependence of bulk properties in the Co-intercalated transition metal dichalcogenide $Co_{1/3}TaS_2$, Phys. Rev. B **109**, L060403 (2024).

[17] S. Wu *et al.*, Highly tunable magnetic phases in transition-metal dichalcogenide $Fe_{1/3+\delta}NbS_2$, Phys. Rev. X **12**, 021003 (2022).

[18] S. Wu *et al.*, Discovery of charge order in the transition metal dichalcogenide Fe_xNbS_2, Phys. Rev. Lett. **131**, 186701 (2023).

[19] S. Mangelsen *et al.*, Interplay of sample composition and anomalous Hall effect in Co_xNbS_2, Phys. Rev. B **103**, 184408 (2021).

[20] H. Tanaka *et al.*, Large anomalous Hall effect induced by weak ferromagnetism in the noncentrosymmetric antiferromagnet $CoNb_3S_6$, Phys. Rev. B **105**, L121102 (2022).

[21] H.-J. Noh *et al.*, Experimental confirmation of the magnetic ordering transition induced by an electronic structure change in the metallic triangular antiferromagnet $Co_{1/3}TaS_2$, Phys. Rev. B **113**, 125126 (2026).

[22] G. D. A. Wood *et al.*, Double-*Q* ground state with topological charge stripes in the centrosymmetric skyrmion candidate $GdRu_2Si_2$, Phys. Rev. B **107**, L180402 (2023).

[23] M. Hirschberger *et al.*, High-field depinned phase and planar Hall effect in the skyrmion host Gd_2PdSi_3, Phys. Rev. B **101**, 220401(R) (2020).

[24] E. Donoway *et al.*, Multimodal approach reveals the symmetry-breaking pathway to the broken helix in $EuIn_2As_2$, Phys. Rev. X **14**, 031013 (2024).

[25] J. A. M. Paddison *et al.*, Cubic double perovskites host noncoplanar spin textures, npj Quantum Mater. **9**, 48 (2024).

[26] J. A. M. Paddison *et al.*, Suppressed-moment 2-k order in the canonical frustrated antiferromagnet $Gd_2Ti_2O_7$, npj Quantum Mater. **6**, 99 (2021).

[27] J. A. M. Paddison *et al.*, Spin dynamics of the centrosymmetric skyrmion material $GdRu_2Si_2$, Cell Reports Phys. Sci. **5**, 102280 (2024).

[28] P. Park *et al.*, Spin dynamics of triple- Q magnetic orderings in a triangular lattice: Implications for multi-Q orderings in general two-dimensional lattices, Phys. Rev. X **15**, 31032 (2025).

[29] R. Kajimoto *et al.*, The Fermi chopper spectrometer 4SEASONS at J-PARC, J. Phys. Soc. Japan **80**, SB025 (2011).

[30] M. Nakamura *et al.*, First demonstration of novel method for inelastic neutron scattering measurement utilizing multiple incident energies, J. Phys. Soc. Japan **78**, 093002 (2009).

[31] Y. Inamura, T. Nakatani, J. Suzuki, and T. Otomo, Development status of software 'Utsusemi' for chopper spectrometers at MLF, J-PARC, J. Phys. Soc. Japan **82**, SA031 (2013).

[32] R. A. Ewings *et al.*, HORACE: Software for the analysis of data from single crystal spectroscopy experiments at time-of-flight neutron instruments, Nucl. Instruments Methods Phys. Res. Sect. A Accel. Spectrometers, Detect. Assoc. Equip. **834**, 132 (2016).

[33] D. Dahlbom *et al.*, Sunny.jl: A Julia package for spin dynamics, Journal of Open Source Software **10**, 8138 (2025).

[34] J. Bezanson, A. Edelman, S. Karpinski, and V. B. J. Shah: A fresh approach to numerical computing, SIAM Rev. **59**, 65 (2017).

[35] E. Kirstein *et al.*, Tunable chiral and nematic states in the triple-Q antiferromagnet $Co_{1/3}TaS_2$, Nat. Commun. **17**, 2212 (2026).

[36] T. Higo *et al.*, Large magneto-optical Kerr effect and imaging of magnetic octupole domains in an antiferromagnetic metal, Nat. Photon. **12**, 73 (2018).

[37] A. L. Balk *et al.*, Comparing the anomalous Hall effect and the magneto-optical Kerr effect through antiferromagnetic phase transitions in Mn_3Sn, Appl. Phys. Lett. **114**, 032401 (2019).

[38] E. Kirstein *et al.*, Topological magneto-optics in the noncoplanar antiferromagnet $Co_{1/3}NbS_2$: Imaging and writing chiral magnetic domains, Phys. Rev. Lett. **135**, 196702 (2025).

[39] Q. Zhang *et al.*, Observation of giant optical linear dichroism in a zigzag antiferromagnet $FePS_3$, Nano Lett. **21**, 6938 (2021).

[40] S. Hayami, Multiple skyrmion crystal phases by itinerant frustration in centrosymmetric tetragonal magnets, J. Phys. Soc. Japan **91**, 1 (2022).

[41] H. Hill, Early actinides: The periodic system's f electron transition metal series, Nucl. Met., Met. Soc. AIME **17**, 2 (1970).

[42] P. Park *et al.*, Quantum and classical spin dynamics across temperature scales in the $S = 1/2$ Heisenberg antiferromagnet, Phys. Rev. Res. **6**, 033184 (2024).

[43] P. Park *et al.*, Anomalous continuum scattering and higher-order van Hove singularity in the strongly anisotropic $S = 1/2$ triangular lattice antiferromagnet, Nat. Commun. **15**, 7264 (2024).

[44] S. Gao *et al.*, Spiral spin liquid on a honeycomb lattice, Phys. Rev. Lett. **128**, 227201 (2022).

[45] C. Kim *et al.*, Bond-dependent anisotropy and magnon decay in cobalt-based Kitaev triangular antiferromagnet, Nat. Phys. **19**, 1624 (2023).

[46] C. Kim, O. Vilella, Y. Lee *et al.*, Kitaev interaction and proximate higher-order skyrmion crystal in the triangular lattice van der Waals antiferromagnet NiI_2, npj Quantum Mater. **11**, 20 (2026).

[47] F. Pedregosa, G. Varoquaux, A. Gramfort, V. Michel, B. Thirion, O. Grisel, M. Blondel, P. Prettenhofer, R. Weiss, V. Dubourg, *et al.*, Scikit-learn: Machine learning in Python, J. Mach. Learn Res. **12**, 2825 (2011).

[48] S. Matin, An opinionated julia wrapper for Bayesian optimization, https://github.com/sakibmatin/BayesOptim.jl.

[49] D. B. Litvin, The Luttinger-Tisza method, Physica **77**, 205 (1974).

[50] A. Little *et al.*, Three-state nematicity in the triangular lattice antiferromagnet $Fe_{1/3}NbS_2$, Nat. Mater. **19**, 1062 (2020).

[51] K. Hwangbo *et al.*, Strain tuning of vestigial three-state Potts nematicity in a correlated antiferromagnet, Nat. Phys. **20**, 1888 (2024).

[52] Q. Tan *et al.*, Observation of three-state nematicity and domain evolution in atomically thin antiferromagnetic $NiPS_3$, Nano Lett. **24**, 7166 (2024).

[53] J. Wagner *et al.*, Magneto-optical study of metamagnetic transitions in the antiferromagnetic phase of α-$RuCl_3$, npj Quantum Mater. **7**, 28 (2022).

[54] Q. Song *et al.*, Evidence for a single-layer van der Waals multiferroic, Nature (London) **602**, 601 (2022).

[55] E. Maniv *et al.*, Antiferromagnetic switching driven by the collective dynamics of a coexisting spin glass, Sci. Adv. **7**, eabd8452 (2021).

[56] Z. Feng *et al.*, Nonvolatile nematic order manipulated by strain and magnetic field in a layered antiferromagnet, arXiv:2507.05486.

[57] J. M. Allred *et al.*, Double-Q spin-density wave in iron arsenide superconductors, Nat. Phys. **12**, 493 (2016).

[58] T. Hatanaka, J. Bouaziz, T. Nomoto, and R. Arita, Calculation of the biquadratic spin interactions based on the spin cluster expansion for ab initio tight-binding models, J. Phys. Soc. Japan **94**, 124709 (2025).

[59] R. Ozawa, S. Hayami, and Y. Motome, Zero-field skyrmions with a high topological number in itinerant magnets, Phys. Rev. Lett. **118**, 147205 (2017).

[60] R. Ozawa *et al.*, Vortex crystals with chiral stripes in itinerant magnets, J. Phys. Soc. Japan **85**, 103703 (2016).

[61] https://www.energy.gov/doe-public-access-plan.